Experiments in Fluids (2026) 67:18
https://doi.org/10.1007/s00348-025-04168-w

RESEARCH ARTICLE

Scalable high-precision silicone models for refractive-index-matched measurements in biomedical applications

Benedikt Harald Johanning-Meiners[1] · **Michael Klaas**[1]

Received: 28 July 2025 / Revised: 14 November 2025 / Accepted: 23 December 2025

Abstract

Introduction Refractive-index-matched (RIM) silicone phantoms play a critical role in experimental biomedical fluid mechanics, enabling detailed investigations of complex flow phenomena in anatomically accurate geometries. However, providing transparent, patient-specific and non-compliant and compliant models for detailed experimental quantitative analysis of the flow field, i.e., with high-dimensional accuracy and minimal post-processing, remains a major challenge.

Methods This work presents a scalable manufacturing workflow based on a wax-based lost-core casting technique. High-resolution wax printing enables the three-dimensional (3D) creation of both non-compliant and compliant silicone phantoms with smooth surfaces, fine structural details, and clean core removal. The method allows for modular assembly of large geometries, and it is demonstrated on three representative models, namely a patient-specific human airway model, a generic compliant bifurcation, and a compliant patient-specific thoracic aorta.

Results Mechanical and geometric tests confirm that the compliant phantoms replicate physiologically relevant vessel properties, with a measured Young's modulus of 1.71 MPa and wall thickness variations below 1%. The phantoms are integrated into flow circuits, and the velocity distribution in the phantoms is measured using volumetric 3D particle-tracking velocimetry (PTV) using the Shake-the-Box (STB) algorithm. Time-resolved measurements under steady and pulsatile inflow conditions reveal detailed flow structures and fluid–structure interactions in both non-compliant and compliant models.

Conclusions The presented workflow enables reproducible, high-fidelity RIM phantoms for experimental studies of biomedical flows. Combined with advanced flow diagnostics, it provides a powerful platform for exploring pathophysiological mechanisms, validating simulations, and evaluating the performance of medical devices in realistic geometries.

1 Introduction

Respiratory, cardiovascular, and vascular diseases represent the most prevalent causes of mortality due to illness on a global scale (Xu et al. 2020). In many of these diseases, fluid-mechanical effects in the human body play a significant role in the course and progression of the disease. Examples include diseases such as chronic obstructive pulmonary disease (COPD), infectious diseases transmitted by inhalation of pathogen-laden aerosols, coronary heart disease, and atherosclerosis. Hence, a deeper understanding of the complex flow dynamics in the human body, e.g., of the airflows in the human respiratory tract or the non-Newtonian blood flow in the elastic blood vessels of the circulatory system often, is an indispensable prerequisite to better understand disease progression or to develop new clinical diagnostic procedures and treatment methods (Nahar et al. 2013). However, a detailed analysis of the fluid mechanics in the human body is often based on *in vitro* studies, which frequently involve numerical methods or experimental techniques, since this approach usually provides full control of the experiment, e.g., in terms of parameter space and temporal and spatial resolution in contrast to *in vivo* investigations, e.g., 4D MRI measurements (Cherry et al. 2022).

For experimental fluid mechanics, refractive-index-matching (RIM) techniques/models in combination with non-intrusive measurement techniques, e.g., laser Doppler velocimetry (LDV), particle image velocimetry (PIV), and particle-tracking velocimetry (PTV), are most frequently used due to their high temporal and spatial resolution.

✉ Benedikt Harald Johanning-Meiners
b.johanning-meiners@aia.rwth-aachen.de

Michael Klaas
m.klaas@aia.rwth-aachen.de

[1] Institute of Aerodynamics and Chair of Fluid Mechanics, RWTH Aachen University, Wüllnerstr. 5a, 52062 Aachen, North Rhine-Westphalia, Germany

Published online: 16 January 2026

Although one of the first RIM experiments by Mcdougall (1979) dates back to 1979, it is still an ongoing challenge to provide accurate flow replicates of, e.g., the human lung, the aortic arch or human blood vessels. Usually, today's experiments still have to overcome the same challenges regarding optical transparency, i.e., high geometrical accuracy, reproducibility, and manufacturing size, especially in the context of biomedical applications. Nowadays, silicone models are used for experiments, for both compliant flow phantoms, e.g., for the analysis of the fluid–structure interaction (FSI) in flexible vessels, and non-compliant models, e.g., for the analysis of the particle deposition and flow structures in the respiratory tract. Matching the refractive index of these silicone models can be easily achieved using a mixture of distilled water (refractive index $n = 1.33$) and glycerol (refractive index $n = 1.47$). However, this approach becomes more challenging when viscoelastic fluid properties, i.e., blood analog fluids, are considered. Moreover, with increasing interest in physiologically relevant experiments, complex three-dimensional geometries are often taken directly from medical imaging data of individual patients (Farkas et al. 2020; Zimmermann et al. 2021). High-resolution, low-noise CT and MRI data have significantly increased the available geometrical complexity of the models, evolving from simple models like the Weibel model (Weibel 1963) to patient-specific designs. This phenomenon becomes even more prominent for experiments that serve as a basis for the validation of numerical simulations, where both the experimental and numerical models have to match very precisely. As far as the experimental models are concerned, this means that model properties like dimensional accuracy, surface quality, optical transparency, refractive index, and wall thickness must be adjusted and controlled within narrow limits. However, previously reported phantom fabrication approaches often suffer from drawbacks that affect the quality and reproducibility of the resulting models, including non-uniform wall thicknesses, surface roughness caused by support residues or limited printing resolution, restricted geometric fidelity in small, branched vessels, and complex or destructive core removal procedures. These limitations directly compromise the accuracy and reliability of subsequent flow measurements.

The present study introduces an alternative workflow that overcomes these issues by employing directly 3D printed wax as a core material. The high printing resolution of 16 µm per layer ensures precise wall definition and optically smooth inner surfaces. Moreover, the solvent-based removal of support material leaves no residue, and the wax core can be extracted cleanly and with minimal effort, even in thin-walled or compliant geometries. The low shrinkage and favorable separation properties of wax further reduce the risk of geometric distortion during demolding, thereby improving the overall accuracy, optical quality, and reproducibility of the manufactured phantoms. In this study, this method is applied to three representative cases, namely a large-scale, non-compliant airway model, a generic compliant abdominal bifurcation phantom, and a patient-specific flexible thoracic aorta model. For larger models exceeding printer volume constraints, the wax core can be segmented and reassembled without compromising dimensional accuracy using form-fitting joints and thermal bonding. While the overall process remains compatible to established lost-core techniques, the use of wax as a printing material offers practical advantages in resolution, scalability, and handling. Therefore, it is a promising alternative for the fabrication of high-fidelity RIM-compatible silicone phantoms in experimental biomedical research.

This manuscript is structured as follows. First, an extensive literature review, divided into two sections, provides a detailed summary of today's manufacturing approaches regarding compliant and non-compliant models used for biomedical RIM experiments. In particular, the limitations, inaccuracies, and difficulties of the manufacturing approaches are described. Consequently, the novel and advantageous manufacturing workflow is explained. Finally, the capabilities of the models are demonstrated by tomographic PTV measurements using the Shake-the-Box algorithm.

1.1 Non-compliant models

Non-compliant or nearly rigid silicone models based on 3D prints are often used to generate realistic airway models, but can also be found for simplified artery models (Wu et al. 2022; Franzetti et al. 2022). However, the experimental analysis of the flow field in airway models is connected to two major challenges. On the one hand, a complete airway model from the upper airways, i.e., oral and nasal cavity, down to the lower airways is considerably large. On the other hand, the complexity of both the upper and lower airways, i.e., the complex structure of the nasal cavity with the turbinates and spurs and the complex bifurcation network of the bronchi and bronchioles with multiple outlets, requires a high spatial resolution of the flow phantom and thus of the core that is used to produce the model. However, increasing the size of the model to improve the spatial resolution during manufacturing often exceeds the limits of the available manufacturing size. In other words, the model cannot be printed as one 3D object. Vice versa, reducing the size of the model to print it in one run often leads to insufficient spatial resolution. Thus, a compromise between these two challenges is often used in the literature. To validate numerical simulations, Cozzi et al. (2017) investigated the flow field inside a 2:1 silicone replica of the nasal cavity of a male patient using stereoscopic (2D/3C) PIV. The geometry of the cavity was reconstructed from a CT scan and manufactured by lost-core

casting using hemihydrated calcium sulfate as the printing material, which was covered with diluted vinyl-based glue to improve the surface quality. Despite capturing small details, removing the printing material was challenging. Similarly, Tauwald et al. (2024) performed phase-locked tomographic (3D/3C) PIV measurements inside a 2:1 model of a patient-specific nasal cavity to investigate the flow structures in the smallest cavities resulting from oscillatory flow. The core for lost-core casting was 3D printed from gypsum powder and a binder, and the core was then coated in 20 layers of polyvinyl alcohol/distilled water solution (PVA) to ensure a smooth surface. Finally, the core was placed inside a rectangular container which was filled with silicone (Sylgard 184) and was then washed out using water. Using tomographic PIV, Nof et al. (2020) analyzed the flow in a generalized mouth–throat airway model made from polydimethylsiloxane (PDMS) to study the effect of invasive mechanical ventilation. The experimental results were also correlated with numerical simulations, indicating that high-frequency ventilation (HFV) reduces the impact of jet impingement on the tracheal bifurcation. The core of the airway model was manufactured on an stereolithography (SLA) printer with a layer thickness of 25 µm. The printed core was spray-painted with clear lacquer to smooth the surface. Finally, the core was washed out by dissolving the core in acetone for 72 h after polymerization of the PDMS. A comparable geometry was investigated by Zhu et al. (2020) to determine the flow field and the flow patterns resulting from realistic inflow curves from obstructive sleep apnea–hypopnea syndrome (OSAHS) using standard 2D/2C PIV. The study suggests that the area of the stenosis is prone to blockage due to potential wall collapse induced by the high-speed jet during peak inspiration. A negative mold was printed from water-soluble materials on an fused deposition modeling (FDM) printer and coated with PVA as a separating agent so that the negative model could be separated from the silicone. The flow field in the lower airways was investigated by Janke et al. (2017) and Soodt et al. (2013) using 3D PTV and stereo-scanning PIV (3D/3C), respectively, revealing a symmetrical and laminar velocity profile upstream of the carina and the prominent recirculation area in the left main bronchus. In both studies, a positive core of a simple lower airway system was manufactured and casted in silicone and washed out consequently.

Apart from the experimental analysis of the flow field in the human respiratory tract, also hemodynamic studies of, e.g., cerebral aneurysms (Brindise et al. 2019), carotid arteries (Buchmann et al. 2011), and dissections (Bonfanti et al. 2020), often use the lost-core method and rigid silicone models. Wu et al. (2022) investigated the flow field inside a rigid patient-specific intracranial saccular aneurysm (IA) using tomographic PIV, stereoscopic PIV, *in vivo* MRI, and numerical simulations. The results of the study emphasize the relevance of spatial resolution of the measurement technique to determine flow quantities such as wall-shear stress (WSS) as well as the consequent diagnostic implications for diseases. The geometry of the core was scaled up by a factor of 3.7, and the geometry of the outlets was adapted and finally extended to allow better connection with the test bench. The core was 3D printed from ABS with a layer thickness of 127 µm. The silicone model was casted from PDMS, and the core was dissolved using acetone. Franzetti et al. (2022) studied aortic dissections in a combined experimental and numerical approach to identify relevant fluid dynamical parameters, i.e., turbulent kinetic energy (TKE) or Reynolds shear stress (RSS) for clinical examinations. Therefore, a patient-specific aortic dissection model was directly 3D printed using an SLA printer with a layer thickness of 100 µm and a transparent material (*TuskXC2700T*) with a refractive index of $n = 1.50$. The model had to be post-processed for a smooth surface, i.e., removal of support structures and a polish of the surface (Table 1).

However, the trend moves toward compliant vessels for hemodynamic experimental investigations since the dilatation of the vessel, i.e., fluid–structure interaction plays a dominant role for the flow especially when the complex non-Newtonian behavior of blood is taken into account.

1.2 Compliant models

As mentioned above, several studies indicate that fluid–structure interaction, i.e., the complex relationship between vessel deformation and flow field, possesses a

Table 1 Exemplary overview of non-compliant models for RIM and non-intrusive measurements considered in the literature

	Publication	Geometry	Measurements	Core material	Model material	Resolution
Non-compliant	Cozzi et al. (2017)	Upper airways	2D/3C PIV	Calcium sulfate	Sylgard 184	600×540 dpi
	Janke et al. (2017)	Lower airways	4D PTV	Low melting alloy	PDMS	n/a
	Nof et al. (2020)	Mouth–throat	3D/3C PIV	Aluminum slabs	Sylgard 184	n/a
	Zhu et al. (2020)	OSAHS	2D/2C PIV	PVA	Sylgard 184	100 µm
	Tauwald et al. (2024)	Upper airways	3D/3C PIV	Gypsum powder	Sylgard 184	n/a
	Wu et al. (2022)	IA	3D/3C PIV	ABS	PDMS	127 µm
	Franzetti et al. (2022)	Aortic dissection	2D/2C PIV	n/a	TuskXC2700T	100 µm

significant influence on the spatial and temporal evolution of the flow. For instance, time-resolved 2D/2C PIV measurements of the oscillating flow of a Newtonian fluid in a straight compliant vessel (Pielhop et al. 2015) and a 180° bend resembling the human aortic arch (Pielhop et al. 2014) showed that the wall-shear stress is highly overestimated for non-compliant vessels with values up to 20% during forward flow and that the volume flux amplitude increases by a factor of 2.1 at the vessel outlet compared to the compliant case. Thus, the focus of hemodynamic investigations has shifted toward thin-walled, compliant vessel phantoms.

In general, production methods for compliant vessels can be divided into two different classes depending on whether or not the vessel is optically transparent and thus suitable for refractive-index-matching and PIV or PTV measurements. On the one hand, methods such as the multistep dip-spin coating process by Arcaute and Wicker (2008), Fahy et al. (2014), Mu et al. (2019) and directly 3D printed silicone model using novel materials, e.g., Biglino et al. (2013), Ionita et al. (2014) are state of the art, but cannot provide a transparent silicone flow phantom suitable for these quantitative velocity measurements. On the other hand, a wide range of production methods exist to produce fully transparent flow phantoms for quantitative flow field measurements. Deplano et al. (2016), Meyer et al. (2011), Yagi et al. (2013) and Wu et al. (2025) used a method called *dip coating* for PIV and 3D PTV measurements. A solid core, i.e., made from glass or ABS, is manufactured and coated with a silicone gel. The excess silicone is removed by rotating the model, which is then cured at higher temperature for a short period of time. This routine is repeated until the desired wall thickness of the phantom is achieved. Subsequently, the core is removed using acetone as a dissolver. However, as stated by Wu et al. (2025), it is difficult to ensure a constant wall thickness and the authors reported deviations from the nominal wall thickness along the model length of up to 15%. A rotational molding process uses a defined volume of low-viscosity silicone which is poured into a mold and then rotated to ensure an even distribution of the silicone on the surface. For simplified geometries, e.g., a generic straight vessel used by Burgmann et al. (2009a) for PIV measurements, this method is able to provide flow phantoms with a wall thickness variation of 4%–7% in the circumferential direction. However, this method becomes more challenging for complex arterial geometries, e.g., as shown by Büsen et al. (2017) for a patient-specific aorta model where manufacturing tolerances of the wall thickness were in the range of $\pm$ 0.5 mm, for a nominal wall thickness of 1.5 mm.

The most common method for the production of elastic vessels is the so-called *lost-core* casting. In this method, a solid core is placed inside a female mold with a small defined gap between the core and the mold, which represents the wall thickness of the final model. By changing the size of this gap, very thin-walled vessels and thus physiologically relevant wall thicknesses can be achieved. The gap is filled with liquid silicone, and once the silicone has cured, the solid core must be washed out or removed mechanically with great care, since the model is much more exposed to rupture. Geoghegan et al. (2012) produced a carotid artery with a symmetric stenosis using the lost-core casting method, with deviations from the original geometry from 3 to 5%.

Najjari and Plesniak (2018) investigated the flow structures in a 180° compliant curved artery model under steady and pulsatile inflow conditions using 2D/2C PIV. The refractive-index-matched vessel was made from Sylgard 184 (Dow corning) and possessed a wall thickness of 2 mm $\pm$ 0.28 mm, i.e., $\pm$ 14 %, and an inner diameter of 12.7 mm $\pm$ 0.1 mm. The negative mold was made from 3D printed ABS. To achieve a smooth surface, the mold was coated with a thin layer of Bondo filler 262, sanded with a sandpaper of various grit sizes, and coated with a layer of PVA glue. The core for the final model was produced using a resin-based 3D printer and the positive model was cast in plaster of Paris. The plaster mold was subsequently coated with two layers of polyvinyl acetate (PVA) to smooth the surface.

Yazdi et al. (2019) propose a novel fabrication method for a compliant artery phantom. Although the geometry of the phantom was not complex, they observed internal movement of the core inside the female mold, resulting in considerable deviations of the wall thickness. Hence, both the core and the female mold were manufactured from ABS with additional disk supports at every end, ensuring a higher consistency of wall thickness. Finally, the silicone model was casted using Sylgard 184 resulting in a final wall thickness of 2 mm, with a variable range of 11%–20%. More recently, in Özcan et al. (2023), the fluid–structure interaction of a patient-specific abdominal aortic aneurysm was investigated using PIV and numerical simulations. The study indicates deviations of the vessel wall deformations of up to 27% between the numerical and experimental data under steady flow conditions. The compliant phantom was manufactured using the lost-core casting technique. The mold was printed on a consumer grade FDM 3D printer with water-soluble PVA at a layer thickness of 100 µm, which was then polished with sandpaper of various grit sizes. Finally, the core was dissolved in warm water, resulting in a wall thickness of approximately 2 mm, but no tolerance was reported (Table 2).

In summary, previous approaches for non-compliant models exhibit several recurring limitations. Chemical removal of printing material can induce geometric uncertainties, as prolonged solvent exposure (typically in acetone) has been shown to induce surface swelling and pitting. The limited print resolution and support structures of these core materials constrain geometric fidelity and necessitate extensive post-processing—such as polishing or manual support

Table 2 Manufacturing methods of compliant models for RIM considered in the literature

	Publication	Geometry	Measurement	Method	Resolution	Error
Compliant	Burgmann et al. (2009b)	Straight	2D/2C PIV	Rot. casting	n/a	4%–7%
	Büsen et al. (2017)	Aorta	2D/2C PIV	Rot. casting	n/a	33%
	Geoghegan et al. (2012)	Carotid artery	n/a	Lost-core	600 × 540 dpi	3%–5%
	Najjari and Plesniak (2018)	180° bend	2D/2C PIV	Lost-core	n/a	±14%
	Yazdi et al. (2019)	Ascending aorta	2D/3C PIV	Lost-core	Height: 100 µm	11%–20%
	Özcan et al. (2023)	Abdominal aorta	2D/2C PIV	Lost-core	Height: 100 µm	n/a
	Wu et al. (2025)	Aorta	4D PTV	Dip coating	Height: 300 µm	15%

removal—to achieve optically smooth inner surfaces. These steps may introduce variability in surface quality and accuracy, extend fabrication time, and increase the risk of contamination or damage of the flow phantom, thereby degrading the optical performance and reproducibility essential for quantitative flow measurements.

The fabrication of compliant phantoms reported in the literature faces significant challenges that are comparable to those for non-compliant models, most notably regarding dimensional accuracy. Reported wall thickness deviations of up to 33% highlight the difficulty of achieving geometrically precise, mechanically consistent models using existing fabrication techniques, e.g., dip coating, rotary casting, and lost-core. Dip coating and rotary casting offer a convenient alternative, but yield limited control over wall uniformity. However, as demonstrated in the literature, conventional lost-core implementations still suffer from inaccuracies and process-induced variations. Last, as for the non-compliant models, additional surface-finishing steps are often required to achieve optical clarity, while solvent-based removal of ABS cores through prolonged acetone exposure can cause swelling or residual stress in the surrounding silicone.

Based on these observations, the present study introduces an improved fabrication workflow for both non-compliant and compliant models that directly addresses these challenges. The method employs directly 3D printed wax as a core material, enabling precise wall thickness control, optically smooth inner surfaces, and reliable core removal without prolonged chemical exposure. The following section outlines the workflow in detail and demonstrates its applicability to a variety of geometries.

2 Methods

This section outlines the complete manufacturing chain of the present study, as seen in Fig. 3. First, general remarks and details of each step of the general workflow are presented, i.e., model preparation, core and additional support structures, scalability by soldering, silicone casting, and demolding. This workflow is subsequently applied to three representative non-compliant and compliant models to demonstrate its reproducibility and applicability across different anatomical geometries.

2.1 Digital phantom design

In the following, the general manufacturing workflow of scalable high-precision silicone models is explained in detail. First, details about the digital phantom and the preprocessing steps for the geometry are discussed. Geometric data for experimental models are based on either generic configurations, e.g., straight and curved vessels and bifurcations with analytically specified geometries, such as diameter, wall thickness, and bifurcation angle; or on patient-specific geometries which are based on MRI or CT scans. Generating, processing, and providing the geometric data often requires considerable effort. However, in the following it will be assumed that these data are available in a digital format suitable for producing models, e.g., as an .stp or .stl data set representing the final geometry for the experimental model. Hence, the essential workflow as it is described in the following and depicted in Fig. 3 already starts with a digital representation of the model. For all model types, i.e., compliant or non-compliant and generic or patient-specific phantom geometries, the geometry data first must be translated into a format that allows for the generation of a negative of the geometry or a male and a female section.

In the literature, e.g., (Geoghegan et al. 2012; Cozzi et al. 2017; Tauwald et al. 2024), anatomical models are frequently enlarged to improve the spatial resolution achievable during fabrication, which is often limited by the layer thickness of the 3D printer used for producing the model negative or mold. However, upscaling is not solely a consequence of limited printing resolution. For complex biological structures with slender or weakly supported branches, geometric enlargement can be crucial to ensure mechanical stability during casting and handling, as small features may otherwise deform or collapse under their own weight when permanent internal supports cannot be introduced. Nevertheless, scaling the model can also be a trade-off: dynamic similarity cannot be maintained arbitrarily. Scaling by large

factors would require correspondingly lower flow velocities or modified working fluids to preserve Reynolds and Womersley numbers, which is particularly challenging for refractive-index-matched mixtures designed to replicate the behavior of non-Newtonian fluids, such as the shear-thinning properties of blood. Moreover, large-scale models rapidly become impractical due to the increase in silicone consumption, printing, and overall manufacturing time, making fabrication prohibitively expensive. Consequently, the model design must balance geometric fidelity, mechanical stability, manufacturability, cost, and dynamic similarity, taking into account both the fabrication constraints and the fluid-mechanical requirements of the intended experiments.

2.1.1 Wax core and support structures

In this study, the model cores, i.e., the positive molds, are printed on an SLA printer (ProJet MJP 2500W) using wax (Visijet M2 Cast) as the printing material. In principle, the only disadvantage of using wax as the printing material for the positive mold is the shrinkage that occurs during cooling from the liquid state. However, this effect can be largely neglected when the wax mold is directly 3D printed with high accuracy and thin layer thicknesses. While the use of wax-like materials for lost-core manufacturing in refractive-index-matched applications is conceptually straightforward, conventional casting of liquid wax often leads to substantial volumetric shrinkage and geometric distortion. These limitations can be reduced for rigid resins such as Araldite, which are suitable for simple geometries but cannot be removed from more complex structures such as bifurcations. Direct 3D printing of wax cores overcomes these issues by eliminating this shrinkage-induced deformation. The resolution of the current printer is $1200 \times 1200 \times 1600$ *DPI* with a layer thickness of 16 µm resulting in a high-precision replica of the digital data set. According to the technical data sheet, Visijet M2 Cast is 100% wax with a density of $0.80\,\mathrm{g\,cm^{-3}}$ at 80 °C and a linear shrinkage of 0.70%. The printing of the positive mold often requires temporary support structures to stabilize overhanging or weakly connected regions, particularly in highly branched or complex biomedical geometries. These supports are essential to maintain dimensional accuracy and to prevent deformation or collapse of fine features. In conventional approaches, both the core and support structures are typically printed from the same material/thermoplastics, for example ABS. In such cases, the supports must be mechanically removed, and the resulting surface irregularities are subsequently smoothed using acetone treatment, as the printed surface quality is too rough for casting silicone models suitable for PIV measurements, Yazdi et al. (2019). While this process effectively improves surface quality, it is difficult to control, as acetone is also used in a later step to dissolve the ABS core from the surrounding silicone. Consequently, the same chemical process that smooths the surface can simultaneously affect dimensional accuracy, which is particularly relevant regarding wall uniformity for compliant models. In contrast, the present workflow employs a secondary wax material for the support structures, which can be dissolved chemically without mechanical intervention, enabling residue-free removal and optically smooth surfaces ideal for refractive-index-matched experiments. The support material is printed in a porous structure that promotes rapid solvent infiltration and thus efficient dissolution. Therefore, the printed parts with the temporal support structures attached are placed in a glass container filled with isopropyl alcohol, which is magnetically stirred and maintained at approximately 30 °C. The dissolution of the wax is primarily governed by the mass transfer, where the concentration of wax in the solvent is determining the rate of removal. Active convective mixing enhances the removal of the support wax, while the elevated temperature increases solubility and accelerates diffusion within the solvent. To further improve the effectiveness of the process, the cleaning is performed in two consecutive steps. In the first stage, more than 90 % of the support wax is removed. The solvent is then renewed, and a second cleaning cycle is carried out to dissolve the remaining traces of support wax. This iterative approach ensures complete removal even in narrow or enclosed regions of complex geometries. Figure 1 illustrates the removal process for two different non-compliant sections of the human respiratory tract model, namely the oral and nasal cavities and the lower airways from the trachea to the 6th bifurcation generation. This efficient removal process is particularly advantageous for thin sections, such as the upper nasal passage of the nasal cavity, where the thickness of the core is less than 0.5 mm. Conversely, when using ABS or similar materials, removing internal supports in narrow areas is nearly impossible without harming the surrounding structure, highlighting the advantage of the wax-based method for intricate, high-resolution designs. Figure 1 (center and right) demonstrates both the necessity and the efficiency of the temporary support structures and their removal for the case of the lower human airways.

Because the diameter of the smallest bronchi of that model is in the order of millimeters and due to the comparably large weight of the funnels connecting the outlets, these parts can be very fragile. Hence, to prevent these parts from breaking apart, it is recommended to attach additional permanent support structures which stay attached to the final model to increase the stability of the model after washout. The permanent support structures can also be seen in Fig. 1. To minimize the contact area between these support structures and the model itself, the permanent structures possess a conical tip with a small contact point. However, having no support structures at all in general is very advantageous since no manipulation of the surface of the core is required

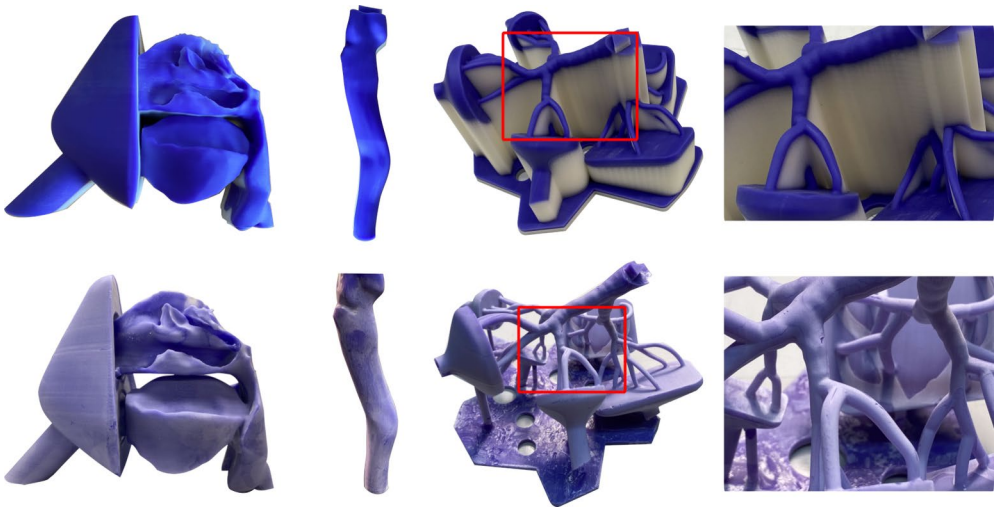

Fig. 1 Temporary, washed-out support structures (white wax) and permanent support structures for two different non-compliant models of the human respiratory tract: oral/nasal cavity (left) and lower airways (center/right)

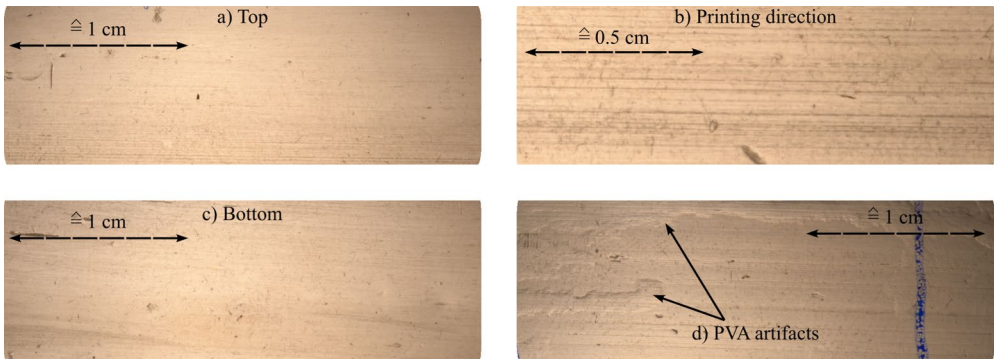

Fig. 2 Four shadowgraphy images of a single casted silicone model. Picture **a** and **c** show regions printed with and without temporary support structures, **b** indicates the printing direction, and **d** irregularities from the PVA coating

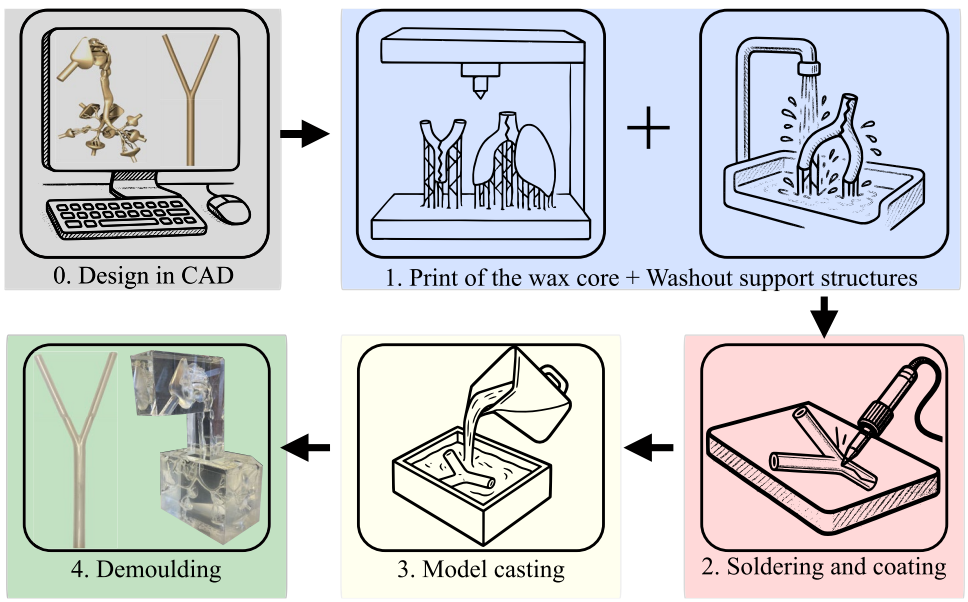

Fig. 3 Generalized workflow for transparent silicone model manufacturing

after the print. To further assess the surface quality and confirm the complete removal of support material, additional shadowgraph measurements were performed on a sectioned mother branch of a bifurcation model (Fig. 2). Illumination was provided by an LED light source diffused through a ground-glass plate, and the images were captured using a 24 MP camera equipped with a 180 mm macro-lens to obtain highly magnified views of the silicone surface. The sample was cut in half to visualize potential surface irregularities through a single silicone layer. The images show both the top (a) and bottom (c) surface including minor artifacts (b) and (d) which can occur during the silicone cast, representing regions printed without and with temporary support structures, respectively. No visible differences or residues of support wax were detected, indicating successful solvent removal. Minor periodic shadows corresponding to the printing direction at the maximum overhang (45°) are visible (c)) but occur only locally and remain negligible for larger scale geometries. Their apparent prominence in Fig. 2 results from the higher magnification of the shadowgraphy images. Fine residues from the manually applied PVA separating layer can also occasionally appear but can be removed by rinsing and reapplication and thus minimized. Overall, the shadowgraphy results confirm smooth, residue-free surfaces suitable for refractive-index-matched flow experiments.

2.1.2 Soldering

Due to the limited build volume of the 3D printer used in this study (294 mm × 211 mm × 144 mm) and to reduce printing time, large geometries were digitally segmented in CAD. Merging these parts into a single model with a classical soldering iron does not alter their geometry. To maintain high geometric accuracy, the parts are connected using form-fitting connectors, such as the triangular connectors shown in Fig. 1 and merged together using a soldering iron. The segments were subsequently joined using a fine-tipped soldering iron at a controlled temperature of 200 °C, with contact times kept below 1 s to avoid deformation of the surrounding printed surfaces. Following assembly, minor surface irregularities at the joints were gently smoothed by localized mechanical polishing to restore geometrical and optical continuity. Finally, a thin and uniform layer of pure polyvinyl alcohol (PVA) separating agent was applied manually with a soft brush to prevent discoloration of the silicone and to facilitate demolding without affecting transparency. The PVA used is a water-thin, alcoholic solution of polyvinyl alcohol that forms a transparent, film-like coating with strong separating properties after drying. To determine the thickness of the PVA separation layer, microscope glass slides were divided into 14 sections, and a thin film of liquid, colorless PVA was applied by brushing. After the PVA was cured, the PVA films were carefully detached from the glass substrate and measured using a micrometer screw. Across the 14 samples, the PVA exhibited an average thickness of approximately 7.5 µm with a standard deviation of 0.73 µm. During application, it should be noted that surface-tension effects can cause locally increased film thickness in regions of high negative curvature, as the liquid tends to accumulate in such areas. Therefore, care must be taken to avoid excessive material buildup when coating complex geometries, as also observed by Geoghegan et al. (2012).

2.1.3 Model casting

For the fabrication of the outer mold, two different approaches were used depending on the model geometry. For the non-compliant models, a simple container made of PMMA was used to hold the silicone during casting, as no precise wall thickness control was required. For the compliant models, such as the bifurcation or patient-specific aorta, a dedicated, contour-following female mold was produced by CNC milling or rapid prototyping to ensure a uniform wall thickness of 1 mm along the entire geometry. PMMA was also used as the mold material in these cases, as it provides optical transparency, and silicone occlusions become easily visible. PMMA provides sufficient dimensional stability, and according to the technical data sheet of the silicone (RTV-615), the cured silicone does not adhere to PMMA, making a release agent unnecessary unless surface polishing or coating is applied. If required, the mold contact surfaces were polished to achieve a smooth finish on the final silicone model and coated with a thin layer of release agent to facilitate demolding. Because of the low viscosity of the silicone, all assembled molds were tested for leakage prior to casting to ensure complete and defect-free filling of the cavity. For the models used in this study, the silicone RTV-615 from Momentive Performance Materials Company GmbH is used. RTV-615 is a two-component PDMS with a moderate viscosity of approximately 4000 mPa s and low shrinkage of less than 2% after curing, which makes it very suitable for the production of refractive-index-matched silicone models. For the casting of the model, the PDMS is precisely weighed to an accuracy of 0.01 g in a 10:1 ratio and thoroughly mixed by hand for five minutes to ensure a homogeneous composition. To prevent overheating and extend the pot life, the use of power mixers is avoided. After mixing, entrapped air is removed by degassing the mixture in a vacuum chamber for approximately 1 h. During this process, the mixture is kept cool by placing cooling packs inside the vacuum chamber alongside the container, maintaining the temperature below 10 °C. The cooling packs are replaced after 30 min to stabilize the temperature and preserve the low viscosity of the silicone, allowing optimal flow around complex features during the subsequent casting. After degassing, the PDMS mixture is temporarily stored in a refrigerator until casting

begins to further extend the pot time. According to the technical data sheet, RTV-615 fully cures within 24 h, although optimal mechanical properties are achieved after seven days. Furthermore, data on the optical transmission coefficient for RTV-615 have been published by Lötters et al. (2014), showing a very high transmission of more than 95% for wavelengths above 400 nm. These results confirm that RTV-615 can be considered optically clear for visible-light applications, which is consistent with qualitative observations of uniform light intensity and the absence of scattering artifacts in the present measurements.

2.1.4 Demolding and core removal

The demolding process represents a critical step in lost-core manufacturing, as improper core removal can compromise the surface quality, transparency, and structural integrity of the silicone model. The procedure differs for compliant and non-compliant models due to their contrasting mechanical and geometric characteristics. Thin-walled compliant models are prone to rupture once even a small cut or micro-defect is introduced, whereas non-compliant models with complex internal geometries and large enclosed volumes are difficult to demold mechanically without risking internal damage.

For compliant models, the removal of the wax core is performed mechanically using a glycerol-assisted separation technique. RTV silicone can rupture from a single micro-defect, especially at thin sections or sharp edges. Therefore, ruptured/teared ends of the silicone model are cut with a very sharp blade to avoid stress concentrations and destruction of the phantom. A long, thin steel tube connected to a syringe is used to inject glycerol between the silicone and the wax interface. The end of the tube is polished smooth to prevent rupture during insertion, as any surface irregularity can easily initiate tearing. Once sufficient lubrication is achieved, the silicone model can be carefully detached from the core without chemical exposure. If necessary, i.e., for branched geometries such as the bifurcation, one daughter branch is carefully separated to enable core removal. This procedure drastically simplifies the core removal while maintaining both the mechanical integrity and the optical quality of the final silicone model.

For non-compliant models, such as the airway geometry, the wax core is first removed mechanically from the silicone model, wherever feasible, to minimize chemical exposure. To prevent damage and maintain the optical quality of the inner surface, this step must be performed with great care. If needed, a small cut can be made in the middle of the model to provide access to both the upper and lower halves of the model, allowing the wax to be gently fractured and extracted without deforming the silicone. However, due to geometric complexity and presence of very narrow cavities, e.g., in the nasal cavity, complete removal of the wax solely by mechanical means is often not feasible. In these areas, the model is therefore placed locally in an unheated ultrasonic bath filled with gasoline at approximately 20 °C. It is known that prolonged exposure ($\mathcal{O}(10\,\mathrm{h})$) of PDMS to organic solvents such as acetone can lead to swelling due to solvent diffusion into the polymer matrix, see Lee et al. (2003). To prevent similar effects, the wax removal process was carefully controlled. Each ultrasonic cycle lasted no longer than 1 min, followed by rinsing with isopropanol and cleaning with pressurized air to remove residual wax fragments. The procedure was repeated as necessary, with a total exposure time of less than 10 min for the given region. After cleaning, the model was air-dried overnight. Under these controlled conditions, no visible swelling, surface irregularities, or loss of optical transparency were observed.

In summary, the presented workflow provides a reproducible and flexible framework for the fabrication of transparent, patient-specific phantoms suitable for any type of RIM measurements. Starting from digital geometries, either generic or patient-derived, the process integrates high-resolution wax printing, controlled silicone casting, and geometry-specific demolding to ensure dimensional accuracy, optical quality, and mechanical integrity. Key aspects for reproducibility are shown in Fig. 3 and include: 1. the direct 3D printing of wax cores and soluble wax support structures to achieve optically smooth inner surfaces, 2. precise assembly of multi-part geometries using form-fitting connectors and coating procedure using PVA, 3. temperature-controlled degassing and casting of RTV-615 to maintain low viscosity and optimal flow properties, and 4. tailored demolding procedures adapted to the mechanical and geometric complexity of the model. This workflow has been successfully applied to fabricate both non-compliant and compliant phantoms, demonstrating its versatility across a range of anatomical geometries and scales. The following sections illustrate the implementation of this process for representative examples, highlighting its clarity, reproducibility, and suitability for experimental flow investigations.

2.2 Exemplary non-compliant model: human respiratory tract

The digital model of the human respiratory tract consists of the upper airways including the nasal and oral cavities, the trachea, and the lower respiratory airways up to the 6th bifurcation generation. For this model, the geometry is based on patient-specific data, see Fig. 4a, derived from CT scans of a healthy 25-year-old male patient. The data set is preprocessed to be suitable for physical airway replicas and CFD simulations and the final geometry was provided by Dr. František Lízal at Brno University of Technology in the form of a .stl file Lizal et al. (2020), Farkas et al. (2020). A medical face mask is added in front of the oral and nasal

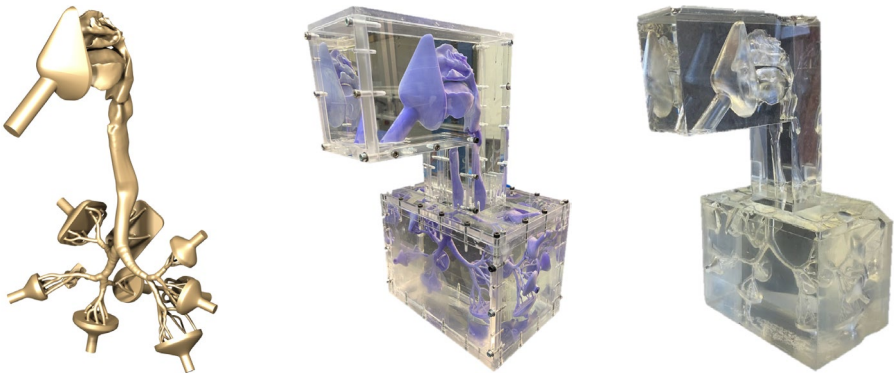

(a) CAD model of the respiratory tract.

(b) 3D printed wax core and casted RTV-615 silicone.

(c) Final PIV model with printing wax removed.

Fig. 4 Simplified workflow of the lost-core method for non-compliant silicone models

ducts to allow individual, i.e., oral or nasal, and combined inhalation and exhalation.

To prepare the digital representation of the respiratory tract for 3D printing, the funnels were adjusted so that the model tightly fits into the casting tank. Additionally, the funnels are designed completely hollow, which reduces the weight and thus improves the stability of the wax core. As depicted in Fig. 1, the respiratory model is divided into four parts, making it easier to reduce the printing time. For better handling, the casting process is divided into two stages: (1) downstream of the first bifurcation generation and (2) the upper airways, including the trachea. The lower airways are first mounted on a suspension system and then lowered into the casting tray. As mentioned in Sect. 2, it takes approximately 7 days for the silicone to fully cure at room temperature. The wax core of the trachea is then connected to the lower airways and the final casting tray is built around the model and filled with silicone. For the non-compliant model, the wax core is removed mechanically from the silicone model, and to ensure that no damage to the model occurs and to guarantee optimal transparency, the wax has to be removed very carefully from the mold. In particular, most of the wax can be removed without destroying the silicone model. A cut is created in the trachea to gain access to the upper and lower airways from both openings. Because the cavities in the nasal region are extremely narrow and mechanical removal may damage the model, only this section is immersed in an unheated ultrasonic bath with gasoline for short, repeated cycles of less than one minute each. The vibration fragments the wax, which is then flushed out using pressurized air. After the wax core is completely removed from the silicone model, both sections are again glued together using a small amount of liquid RTV-615. The final silicone model, e.g., the lower airways and the nasal/oral cavities, can be seen in Fig. 5. The blue discoloration in the image of the upper airway model, Fig. 5 (left), is due to reflections and is not present in the actual model.

2.3 Compliant silicone models

The detailed experimental analysis of the fluid–structure interaction in thin-walled compliant vessel models is one of the major ongoing challenges in hemodynamics. In general, the compliance of thin-walled vessels is managed through properties like the wall thickness of the vessel, the transmural pressure, and the Young's modulus of the vessel material. However, casting a compliant vessel with controlled wall thickness and homogeneous material properties imposes the same requirements for the male core as they are needed for non-compliant models, namely a precise geometry, a smooth surface finish, and reproducibility of the casting process. In the following, this casting routine will be described in

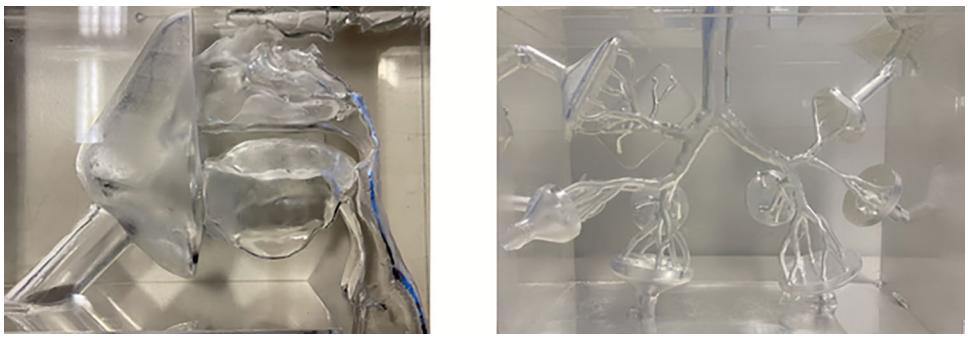

Fig. 5 Close up of the final silicone model. Left: oral and nasal cavities and additional medical inhalation mask; Right: bronchi up to the sixth bifurcation generation

detail for two different compliant vessel phantoms, namely a generic bifurcation mimicking the dimensions and properties of the human abdominal aorta, and a patient-specific ascending aorta model based on CT data.

2.3.1 Generic bifurcation geometry

The generic compliant bifurcation model described below is adapted from Lee and Tarbell (1997) and is analogously scaled up in dimensions by 30 %. The model as it is shown in Fig. 6 possesses an initial inner diameter of $D_0 = 20\,\text{mm}$ for the mother branch, inner diameters of $D_1 = D_2 = 13\,\text{mm}$ for the daughter branches, and a bifurcation angle of $\theta_1 = \theta_2 = 22.5°$. To perform non-invasive static pressure measurements simultaneously to the PIV measurements, three miniature pressure sensor mounts with an inner diameter of 1 mm are embedded in the model. The three sensors are located at $L = 70\,\text{mm} = 3.18 \cdot D_0$ from the junction point of the skeleton line in the mother branch and in each daughter branch. Due to the size of the bifurcation model with an overall length of 395.7 mm, the core is printed in three parts that are soldered together maintaining the nominal opening angle between both daughter vessels. For this purpose, the individual parts of the wax core are placed in the recess of a CNC-milled plate in which the diameter of the recess corresponds exactly to the diameter of the core. In this way, it can be guaranteed that the pieces of the wax core are precisely soldered together. The female mold of the vessel consists of two transparent PMMA plates which are divided in the symmetry plane of the bifurcation model. To ensure the correct offset between the wax core and the female mold and thus a constant wall thickness of the final model, the male core is positioned in the PMMA plate using coaxial positioning rings at the ends of the model. The stability provided by the three positioning rings in combination with the stiffness of the final wax core is sufficient to prevent bending between the PMMA plates.

Analogously to the casting of the non-compliant airway model, a mixture of RTV-615 is prepared (mixing, cooling, degassing) and then slowly poured into the 1 mm gap between the two molds. It is crucial that no air bubbles are trapped, e.g., inside a pressure pin, as this drastically increases the risk of rupture. Once the silicone has cured, the dummy pressure pins are removed, and the male core is washed out using warm water. The demolding becomes easier using a long and thin steel tube connected to a syringe and injecting glycerol between the silicon and the wax core. The final silicone model can then be easily removed from the core.

2.3.2 Patient specific ascending aorta

The manufacturing routine described above becomes different for a patient-specific geometry here shown for a thoracic aorta of a healthy 50-year-old male patient. The geometry was previously used by Zimmermann et al. (2021) to study the effect of increased vessel wall stiffness, employing three models with increasing wall thickness. In a first step, the .stl file must be modified to allow printing a three-dimensional solid wax core, since the original approach was to print the phantom directly. Subsequently, the lengths of the brachiocephalic artery, the left common carotid artery, and the left subclavian artery, as well as those of the ascending and descending aorta, are extended to allow the connection of the final flow phantom to the inlet and outlet pipes of the experimental setup. Due to the size of the model, the core is split into two parts that can be soldered together using form-fitting connectors after the support wax is removed. Since the patient-specific geometry is highly three-dimensional and asymmetric, the separation surface between the two halves of the female mold is not a simple plane (see Fig. 6), but must be adapted to the geometry. Therefore, a complex surface was designed to evenly split the female mold, preventing undercuts and allowing demolding, as shown in Fig. 7. The female mold is produced using a 3D fused deposition modeling (FDM) printer (Raise3D Pro3 Plus HS) with a nozzle diameter of 400 µm and a resulting layer thickness of 100 µm. The contact surfaces are polished to enhance the quality of the silicone model. Similarly to the bifurcation model, coaxial positioning rings are used at each end to keep

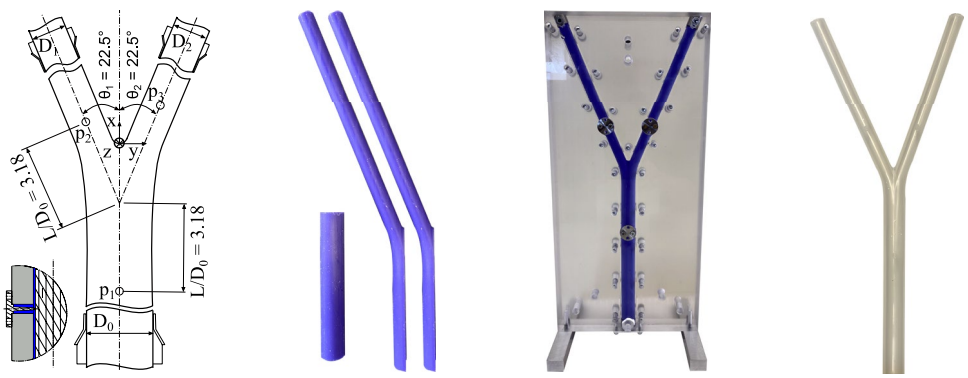

Fig. 6 Simplified workflow of the lost-core method for compliant silicone models. From left to right: sketch of the bifurcation geometry and miniature pressure sensor mounts (final silicone model indicated by blue color); wax core consisting of three parts; assembly of wax core, female mold, and pressure dummies; final silicone model

Fig. 7 Simplified workflow of the lost-core method for the compliant patient-specific ascending aorta, from left to right: .stl file of the core and male wax core; wax core in the female mold; final flow phantom

the model in place and to ensure a constant wall thickness of 1 mm. Finally, the silicone is simultaneously poured into the ascending and descending aorta to prevent air bubbles in enclosed regions inside the mold. The subsequent demolding and core removal follow the same procedure as described for the bifurcation model.

3 Vessel properties: material and geometry

When considering compliant artery models, the structural properties of the phantoms play a significant role in the fluid–structure interaction and thus the resulting flow fields. Learoyd (1966) determined the circumferential incremental Young's modulus of real human arteries by measuring the Young's modulus of 59 major arteries from subjects under 35 ('young') and over 35 ('old') to investigate age-related effects on arterial wall viscoelasticity. These measurements form the foundation of most of today's *in vitro* studies, where the material properties of the arterial walls of *in vitro* phantoms are chosen such that they match the properties of the specimen of that study.

3.1 Tensile tests and dynamic mechanical analysis

In this study, the material properties of the elastic vessels correspond to the values determined by Dörner et al. (2021), who measured the Young's modulus, the storage modulus (E'), and the loss modulus (E'') of RTV-615 (additionally, a small amount of Rhodamine B was added to the mixture to enhance the reflection of the vessel walls) as a function of frequency within the linear viscoelastic range (LVR) at 30 °C. For further details, please refer to Dörner et al. (2021).

The Young's modulus was determined based on three tensile tests at 30 °C using a Z100 tensile test machine. The silicone specimen (DIN 53504 S2) was spray-painted with a speckle pattern to determine the displacement optically for a maximum displacement of 30 mm and an initial load and initial load speed of 0.3 N and 30 mm s^{-1}. The Young's modulus was determined to be $E = 1.71$ MPa in a strain range of $0.02 \leq \epsilon \leq 0.08$, with $\epsilon = ln(L/L_0)$. The stretched tensile length is indicated as L and the initial length as L_0, see Dörner et al. (2021). The material showed strong hysteresis, with delayed relaxation and possible permanent distortion, determined for strains up to $\epsilon = 0.54$.

The time-dependent properties of nine different specimens were measured in a dynamic mechanical analysis in the range between [0.2 h, 10 h] using a TA Instruments DMA Q800. The applied dynamic strain $\gamma(t)$ was defined as $\gamma(t) = \gamma_0 \cdot sin(\omega t)$, with γ_0 denoting the dynamic strain amplitude and ω the angular frequency. The dynamic stress response was defined as $\sigma(t) = \sigma_0 \cdot sin(\omega t + \delta)$, with σ_0 as the dynamic stress amplitude and δ as the phase offset between the stress and strain waves. As a result, the complex modulus was calculated as $|E^*| = \sigma_0/\gamma_0$. Finally, the storage and loss modulus was calculated using $E' = |E^*| \cos(\delta)$ and $E'' = |E^*| \sin(\delta)$. Figure 8 left shows both E' and E'' plotted against the frequency within the LVR for RTV-615 in comparison to the data from real young and old abdominal arteries by Learoyd and Taylor (1966). The comparison between the silicone and the data of a real vessel in the frequency range of 2 Hz–10 Hz shows very good agreement for the storage modulus, whereas the loss modulus deviates slightly from young and old patients. In conclusion, the silicone vessel model accurately replicates the elastic properties of large human vessels and qualitatively captures the damping behavior at various frequencies (Dörner et al. 2021).

3.2 Wall thickness measurements

To determine the accuracy of the casting process of the compliant models with respect to the wall thickness of the flow phantoms, the wall thickness of the bifurcation model is measured in detail. First, the bifurcation is separated into three sections: one mother branch and two daughter branches. The three sections are cut equidistantly into 3 mm rings using a CNC lathe. Next, each ring is placed on a rotating table and the inner and outer diameter of each ring is measured using the optical viewfinder of a CNC milling machine. The edges of the silicone ring are tracked using the crosshair and the inner/outer vessel diameter is measured

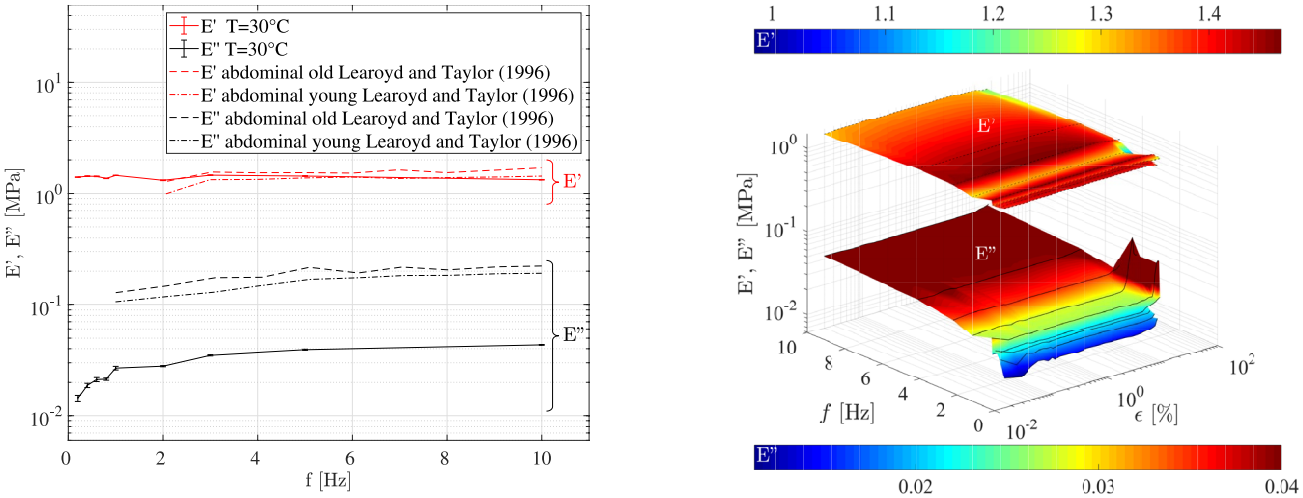

Fig. 8 Storage and loss modulus of a silicone specimen and a real human blood vessel from Learoyd and Taylor (1966) as a function of the frequency and strain (Dörner et al. 2021)

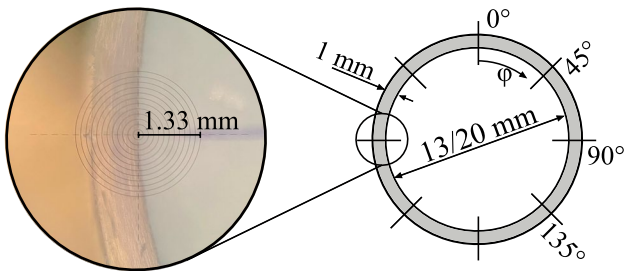

Fig. 9 Overview of the viewfinder and cut segments of the bifurcation model

by vertical translation, resulting in a measurement accuracy of 0.01 mm. An exemplary image of the wall thickness measurement and a sketch of the measurement positions are shown in Fig. 9. In total, the wall thickness of the silicone model and consequently the resulting inner and outer diameter is measured for each segment at four circumferential positions with a circumferential spacing of 45°.

Figure 10 shows the normalized mean outer ($'o'$) and inner ($'i'$) diameters of the mother branch ($d_{o,M}$ and $d_{i,M}$; top left) and the two daughter branches ($d_{o,D1}$, $d_{i,D1}$, $d_{o,D2}$, and $d_{i,D2}$; top right), as a function of segment index (cut locations along the branch). Figure 10 bottom depicts a schematic of the mother branch (extending between $x_0 = 0 \rightarrow x_1 = 25\,\text{mm}$) and the two daughter branches (extending between $x_2 \rightarrow x_3$). The inner and outer diameters are measured for the two given intervals. As indicated by the plots, the maximum deviation of the outer and inner diameters from the nominal values is less than 1%. This small variation shows that the wall thickness and the overall vessel diameter remain nearly constant over the length of the branches and consequently the accuracy of the manufacturing method thus ensuring reliable and repeatable flow characteristics for flow field measurements.

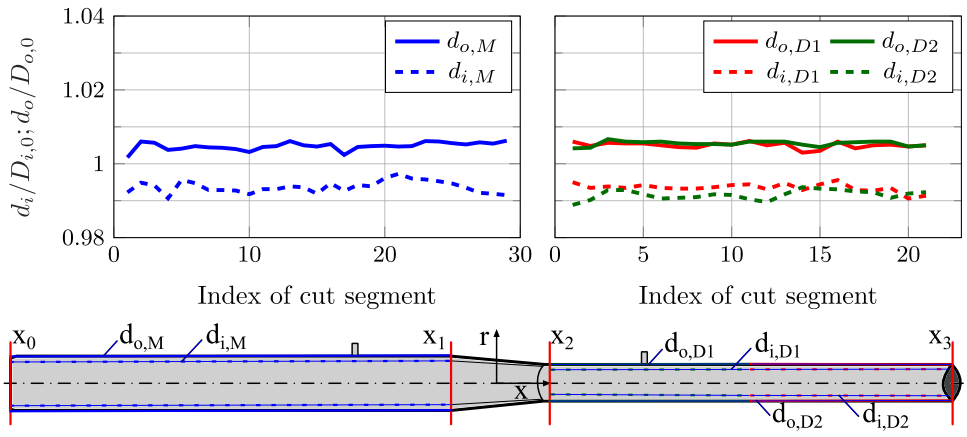

Fig. 10 Wall thickness measurement of the bifurcation model. Top left: mean outer/inner diameter of the mother branch normalized by the nominal diameter $D_{o,0} = 22\,\text{mm}$ and $D_{i,0} = 20\,\text{mm}$ Top right: mean outer/inner diameter of the daughter branches normalized by the nominal diameter $D_{o,1,2} = 15\,\text{mm}$ and $D_{i,1,2} = 13\,\text{mm}$

4 Exemplary results: tomographic PTV measurements

This section presents exemplary time-resolved volumetric velocity measurements based on three-dimensional particle-tracking velocimetry (3D PTV) using the Shake-the-Box (STB) algorithm for both the compliant and non-compliant flow phantoms to demonstrate their suitability for refractive-index-matched velocity measurements. The non-compliant airway model is embedded into a closed-loop circuit with a continuous pump simulating steady and calm inhalation at a Reynolds number of Re = 400. The two compliant artery models are embedded into an open circuit to simulate pulsatile inflow conditions. The pulsatile waveform for the generic bifurcation is adapted from generic waveforms measured by Olufsen et al. (2000) and yields a Reynolds number of Re = 2000 and a Womersley number of Wo = 20. For the patient-specific aorta model, the corresponding patient-specific waveform is scaled to match a Reynolds number of Re = 1000 and a Womersley number of Wo = 14. Both measurement fluids for the compliant and non-compliant measurements are seeded with *Orgasol* particles often used in Tomo PTV applications using the STB algorithm, see Schröder et al. (2020) with a mean diameter of 47.7 µm resulting in a maximum Stokes number of $\mathrm{St}_{\max} = 5 \cdot e - 4$. Due to the three-camera setup used in the measurements of the airway model, a lower seeding density of approximately 0.03 *ppp* was used. Due to the nature of the experimental setup, the airway model was submerged in a tank filled with the same measurement mixture of water/glycerin, and a laser was used instead of a light-emitting diode (LED) system to more precisely guide the light beam into the measuring section. In contrast, for the measurements of the compliant artery models, a higher seeding density of up to 0.06 *ppp* was applied and the models were submerged into a non-seeded mixture of the same measurement fluid. Lastly, the seeded measurement mixtures were left to rest overnight, allowing particles with slight buoyancy or excessive settling tendencies to separate. After this period, only the neutrally suspended particles remaining in the bulk of the fluid were used for the measurements. The study did not observe occlusion effects, wall effects, or sensitivity to pulsatile motion due to transparent, refractive-index-matched silicone models and optimized camera alignment ensuring clear visibility. Although calibration outside the model could affect reconstruction geometry, minor optical path changes from wall deformation were negligible. No motion-induced distortions or artifacts were detected in processing. In both cases, the volumetric measurements are processed using the software DaVis 10 by LaVision.

4.1 Tomographic PTV measurements in a patient-specific airway model

The Tomo PTV measurements use a refractive-index-matched mixture of water and glycerin as the measurement fluid. The mixture consists of 56.75 wt% glycerin and 43.25 wt% of distilled water, resulting in a density of $\rho_{WG} = 1.139\,\mathrm{kg\,m^{-3}}$ and a dynamic viscosity of $\eta_{WG} = 6.9\,\mathrm{mPa\,s}$ for a temperature of $T_{WG} = 30\,^{\circ}\mathrm{C}$. The water/glycerin mixture inside the measurement tank is temperature-controlled ensuring a constant refractive index, density, and viscosity of the measurement fluid throughout the experiments (Fig. 11).

To generate defined inflow conditions, i.e., a fully developed velocity profile upstream of the mask, and to enable a comparison with numerical data, a straight inlet pipe with a hydraulic diameter of $d_i = 20\,\mathrm{mm}$ and a length of $L_i = 1640\,\mathrm{mm} = 82 d_i$ is installed upstream of the mask. The inlet velocity profile upstream of the mask is measured using a low-speed (LS) PIV system consisting of a Continuum Minilite laser and a PCO edge sCMOS camera with a 100 mm lens to determine the volume flux and thus the Reynolds number in the trachea. The PTV images are captured using three high-speed cameras: one Photron Fastcam NOVA S12 positioned at 0° and two Photron Fastcam Mini WX100 placed at ± 25°. These cameras are equipped with 100 mm Zeiss lenses and are positioned approximately 800 mm from the measurement volume. To illuminate the region of interest, an approximate volume of $25 \cdot 25 \cdot 50\,\mathrm{mm^{-3}}$, a 100 mJ Nd: YLF Darwin-Duo laser with a wavelength of $\lambda = 527\,\mathrm{nm}$ is equipped with a volumetric optic (LaVision). Due to the three-camera setup and thus to further minimize distortion effects, the measurement tank is designed with walls perpendicular to each camera. The two Photron Fastcam Mini WX100 cameras are Scheimpflug corrected, achieving a spatial resolution of $19.5\,\mathrm{px\,mm^{-1}}$. To ensure a sufficient depth of field (DOF) across the entire measurement volume, an aperture setting for the three cameras of $N_{\mathrm{Mini}} = f/16$ and

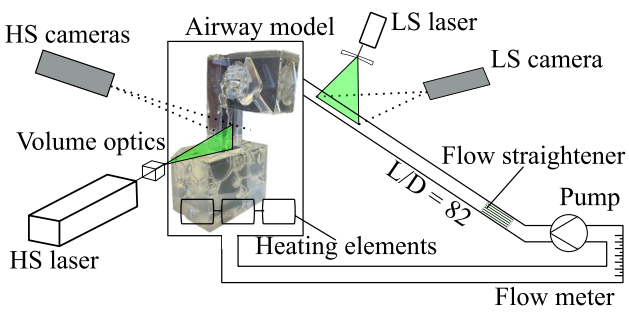

Fig. 11 Experimental setup for the steady 3D PTV measurements of the non-compliant model of the human airways

$N_{\text{Nova}} = f/22$ is chosen, resulting in a lower bound of the depth of field of DOF $\approx 2 \cdot N \cdot c \cdot (u/f)^2 \geq 28\,\text{mm}$, with c as the circle of confusion, u the distance to the subject and f the focal length. This adequately covers the full illuminated region of interest and ensures that all particles remain in sharp focus throughout the measurement volume. The PTV images were captured at a single exposure frequency of 619 h resulting in maximum particle shift of 10 px, as recommended by Schanz et al. (2016). The mapping was obtained using a third-order polynomial fit, followed by a volume self-calibration routine. The volume self-calibration was conducted with the same particle density (approximately 0.03 *ppp)*, frame rate, and exposure as in the experiments. The self-calibration was performed iteratively until the maximum disparity error was reduced below 0.1 *vx*, ensuring subpixel accuracy. A final average disparity of 0.04 vx was achieved. The volume self-calibration yields a final maximum calibration fit error of 0.0099 px across the three cameras. While the three-camera configuration for the airway model doesn't meet the typical four-camera standard in tomographic PTV, it was optimized to reduce reconstruction ambiguity and ghost-particle formation. To address the decrease in views, a low seeding density of 0.03 ppp and a minimum track length of five time steps were utilized during acquisition and processing, as recommended by Schanz et al. (2016). This approach provides sufficient particle correspondence and reliable 3D reconstruction, while maintaining a favorable signal-to-noise ratio and stable tracking performance. For the processing of the tomographic PTV measurements, a triangulation error of 1.5 *vx*, a shake width of 0.11 *vx*, a particle intensity threshold of $0.1 \cdot I_{\text{avg}}$, and a minimum track length of five steps were employed to further reduce ghost particles. Finally, a spatial median $3 \times 3 \times 3$ filter was applied to suppress false particle tracks. Without using an ensemble averaging approach, initial tests showed that a seeding density of around 0.03 ppp provided the most consistent results for the three-camera setup. To further quantify the possible measurement error, the uncertainty of the absolute velocity is calculated to be lower than $|V| \pm 0.005$ m/s.

Figure 12 illustrates the orientation and position of the coordinate system for the PTV measurements. The coordinate system (X, Y, Z) is scaled using the hydraulic diameter of the trachea $d_{\text{TR}} = 16.3\,\text{mm}$, originating at the bronchial bifurcation of the two main bronchi with y^* pointing upwards into the trachea. The x^*y^*, y^*z^*, and x^*z^* planes correspond to the coronal, sagittal, and transverse planes, respectively. For more details, see Johanning-Meiners et al. (2024). Figure 12 shows the 3D particle tracks color-coded by the velocity amplitude. The tracks are cropped along the sagittal plane for better visualization of the inner flow phenomena. The skewed velocity profile indicates the high-speed jet of the trachea, while secondary flow phenomena from the upper airways and the three-dimensional geometry of the model can be seen in the lower section of the measurement volume. A small section of the particle tracks is missing approximately in the center of the measurement volume due to a visible edge in the silicone model, caused by the model being cast in two consecutive stages.

4.2 Tomographic PTV measurements in compliant vessels

Figure 13 shows an exemplary sketch of the experimental setup for an elastic vessel. The silicone model, in this case the bifurcation, is placed inside a large measurement tank that is filled with the same refractive-index-matched fluid as it is used for the experiments. Measurements using both Newtonian and non-Newtonian fluids are presented for the bifurcation and the aorta, respectively. The Newtonian fluid is a composition of distilled water, glycerol, sodium iodide, and sodium thiosulfate. The viscoelastic characteristics of the non-Newtonian blood analog are replicated by adding xanthan gum to the mixture. The composition of both fluids

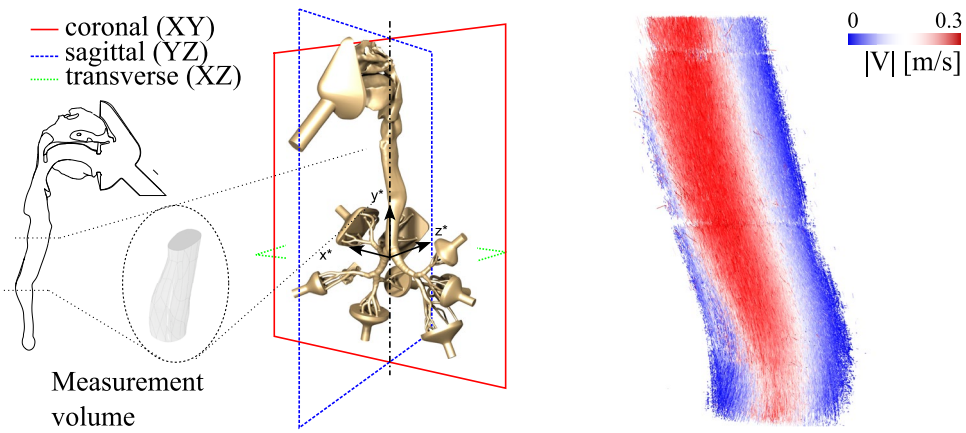

Fig. 12 Measurement domain of the airway model and 3D particle tracks of stationary oral inhalation for Re = 400; colormap: velocity magnitude

Table 3 Composition and properties of NF and NNF solutions

Ingredients		NF	NNF
Distilled water	[wt %]	48.99	53.45
Glycerol	[wt %]	36.94	22.92
Sodium iodide	[wt %]	13.97	23.51
Sodium thiosulfate	[wt %]	0.1	0.1
Xanthan gum	[wt %]	–	0.02405
Density $\rho_{30\,^\circ\mathrm{C}}$	[kg/m^3]	1222.5	1285.7
RI $n_{30\,^\circ\mathrm{C}}$	[–]	1.4077	1.4077

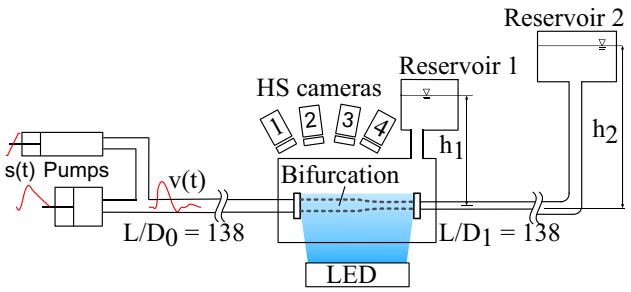

Fig. 13 Experimental setup for the 3D PTV measurements of the compliant bifurcation

is listed in Table 3. For more details, i.e., viscosity curve, mixing procedure, please refer to Dörner et al. (2021).

Straight long pipes with $L/D_{i,0} = 138$ (L: length, $D_{i,0}$: inner diameter) up- and downstream of the measurement tank ensure a fully developed inflow velocity profile. Two reservoirs placed at two different heights are used to generate a transmural pressure difference of $p_{\mathrm{trans}} = \rho \cdot g \cdot \Delta H = 12467\,\mathrm{Pa}$, thus ensuring a higher static pressure inside the vessel compared to the pressure in the measurement tank. Reservoir 2 has an overflow weir ensuring a constant height even for the positive volume flux resulting from the pulsatile flow. The temperature of the measurement fluid is kept constant at 30 °C using six active temperature controllers and heating cables to keep the density, viscosity, and refractive index constant during the experiments. Finally, the volume flux is realized by two precision motors with an active position feedback, which are connected to two individual piston pumps. The first pump realizes a cyclic motion, which is superimposed by a second linear pump resulting in a high-precision waveform. The PTV setup consists of four Phantom v2640 cameras equipped with Zeiss 100 mm macro lenses and two LED systems for the volumetric illumination of the complete model. The Reynolds number $\mathrm{Re} = (\rho_{\mathrm{NF}} \cdot |\overline{u_B}| \cdot D_{i,0})/\eta_{\mathrm{NF}}$ is calculated using the absolute value of the maximum bulk velocity $|\overline{u_B}|$, the inlet diameter of the bifurcation model $D_{i,0}$, and the density and dynamic viscosity of the measurement fluid $\rho_{\mathrm{NF},30\,^\circ\mathrm{C}}$ and $\eta_{\mathrm{NF},30\,^\circ\mathrm{C}}$, respectively. The Womersley number reads: $Wo = (D_{i,0}/2) \cdot \sqrt{(\omega \cdot \eta_{\mathrm{NF},30\,^\circ\mathrm{C}})/\rho_{\mathrm{NF},30\,^\circ\mathrm{C}}}$, with ω as the oscillation frequency, and again η_{NF} as the dynamic viscosity and ρ_{NF} as the density of the Newtonian fluid at 30 °C. To ensure comparable flow conditions for Newtonian and non-Newtonian fluids, the blood analog fluid experiments use the same piston pump parameters, i.e., frequency and stroke volume. The acquired particle images from the experiments are preprocessed by subtracting the moving average of 13 images because of the vessel movement. Subsequently, a multilevel target calibration routine is applied as well as the volume self-calibration, yielding a final average disparity of 0.01 vx and 0.04 vx for the Newtonian and the non-Newtonian fluid, respectively, through four types of media, i.e., air, glass, measurement fluid, and the silicon model. Although a four-camera setup is less prone to observe ghost particles and, in general, a better volumetric reconstruction can be achieved, to ensure high reconstruction fidelity, a triangulation error of $\epsilon = 1.0$ vx was applied for NF case and $\epsilon = 0.7$ vx for the NNF cases due to the lower signal-to-noise ratio. For both configurations, a shake width of $\delta = 0.11$ vx was used. To further suppress ghost-particle artifacts, the minimum track length was set to five for the NNF cases.

Figures 14 and 15 show time-resolved three-dimensional particle tracks for the generic bifurcation and the patient-specific aortic arch for different timestamps of a cardiac cycle. While Fig. 14 depicts the velocity field in the bifurcation for the early and peak systole, Fig. 15 shows the velocity distribution in the aorta for the peak and late systole. The bifurcation waveform is adapted from Olufsen et al. (2000) and possesses a Reynolds number of Re = 2000 and a Womersley number of Wo = 20. The waveform for the aorta is based on the patient-specific waveform provided by Zimmermann et al. (2021) with Re = 1000 and Wo = 14.

To better visualize the flow phenomena perpendicular to the main flow direction in the mother branch, the upper half of the particle tracks is cropped at $z = 0\,\mathrm{mm}$ in the symmetry plane of the bifurcation. Figure 14 (left) shows the velocity component in y-direction, and Fig. 14 (right) shows the velocity magnitude $|V| = \sqrt{u^2 + v^2 + w^2}$. During early systole, flow reversal occurs from the daughter branches into the main artery. The velocity in the y-direction emphasizes the model's symmetry, showing zero velocity along the stagnation point axis, where both branches meet. The diameter of the mother branch significantly increases from early systole with $d_{i,M} = 20.8\,\mathrm{mm}$, i.e., 4% to $d_{i,M} = 24.1\,\mathrm{mm}$, i.e., 20.5% during peak systole, while the maximum absolute velocity remains below $0.1\,\mathrm{m\,s^{-1}}$. Due to the compliance of the vessel, energy is used primarily for vessel expansion, creating four recirculation regions in the main branch.

The three-dimensional particle tracks of the absolute velocity inside the patient-specific aorta can be seen in Fig. 15. At peak systole, a strong recirculation region can

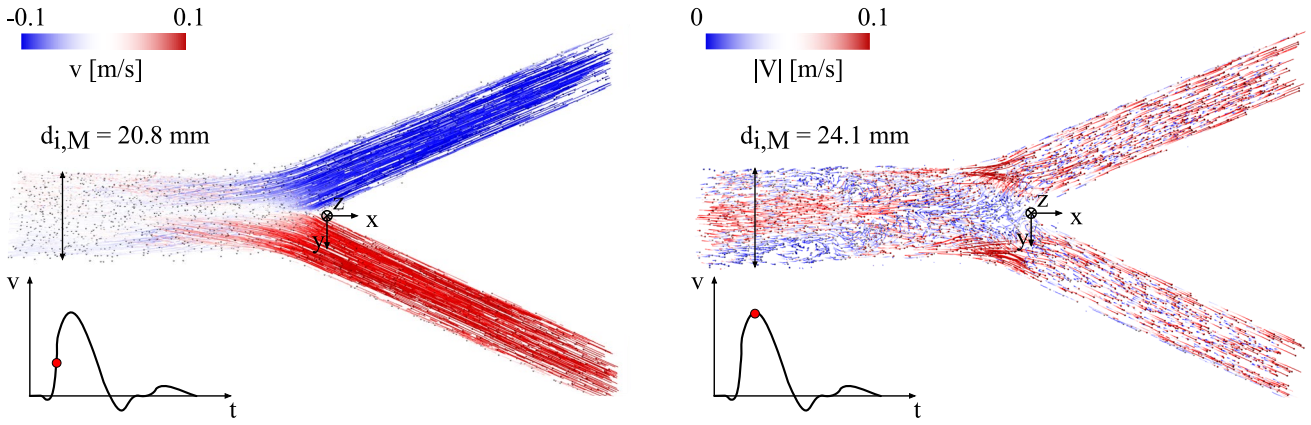

Fig. 14 Time-resolved 3D particle tracks clipped at $z = 0$ mm at two timestamps of a cardiac cycle for a Newtonian fluid, for Re = 2000 and Wo = 14; colormap: velocity component v in y-direction (left) and velocity magnitude $|V|$ (right)

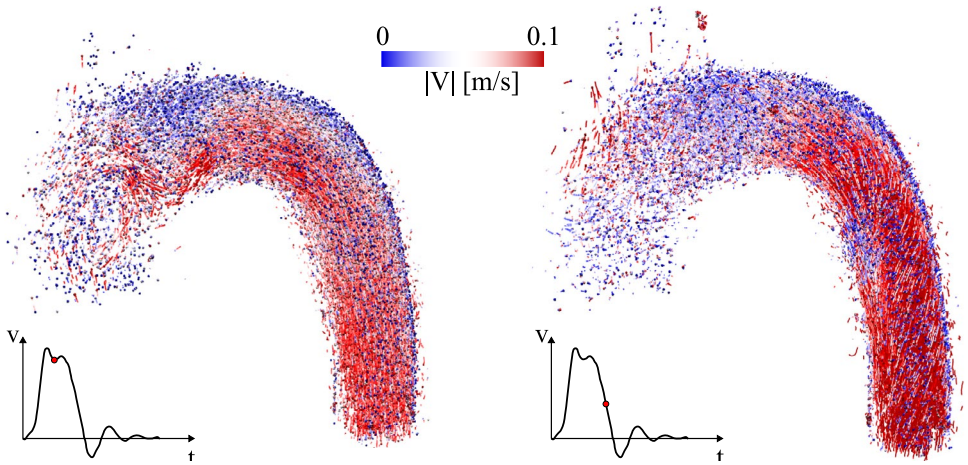

Fig. 15 Time-resolved 3D particle tracks at two key timestamps of a cardiac cycle (left: peak systole flow; right: Late systole flow) for a non-Newtonian fluid; colormap: velocity magnitude

be observed right downstream of the bulbus. However, it dissolves into an m-shaped high-speed region concentrated along the inner curvature of the vessel. Similar to the dilatation of the bifurcation vessel, the kinetic energy of the flow is converted into potential energy, resulting in a dilatation of the vessel. Consequently, the highest velocity amplitude is not reached at this point of the cardiac cycle, but during the late systole. A high-speed region downstream of the point of inflection and secondary flow phenomena induced by the curvature of the vessel can be seen in Fig. 15 right.

5 Conclusion

This work introduces and validates a wax-based lost-core casting method that allows precise, large-scale manufacturing of both non-compliant and compliant silicone models for refractive-index-matched biomedical flow studies. By 3D printing the core from high-resolution wax, support material is removed residue-free, minimizing post-processing while preserving fine and small-scale features with high accuracy. The direct soldering of wax segments enables up-scaling to large patient-specific geometries. The workflow of manufacturing a non-compliant airway model and two compliant silicone models, namely a generic bifurcation model and a patient-specific aorta, is presented. For the compliant artery vessels, the material properties are presented by means of tensile tests and a dynamic mechanical analysis. A Young's modulus of $E = 1.71 \times 10^6$ Pa and the complex storage and loss modulus of a silicone specimen are measured. The wall thickness of the compliant bifurcation model was measured using the optical viewfinder of a CNC milling machine and evidencing deviations in the wall thickness of less than 1% along the mother and daughter branches. Finally, the manufactured models are embedded into flow circuits and volumetric measurements using the Shake-the-Box algorithm are performed, which underline the accuracy of the model and compliant behavior of the elastic vessels. As far as the current models are concerned, the measurement

results presented in this paper are just excerpts from a detailed flow analysis for future investigations.

The entire airway system from the upper airways down to the sixth bifurcation generation can be investigated, giving new insights into the flow field, e.g., the influence of physiological oral and nasal inhalation on the lower airways. The study shows that it is possible to combine multiple casts of silicone, as shown for the airway system, yet, distortions inside the model can occur.

The flexibility of the proposed method enables the fabrication of models replicating a wide range of patient-specific pathologies, including deviated nasal septum, obstructive sleep apnea–hypopnea syndrome (OSAHS), stenoses, aneurysms, and vascular malformations. Additionally, the method can be leveraged to embed or interface with medical devices (e.g., stents, valves, cannulas) within the models to experimentally investigate device-tissue interaction under physiologically relevant flow conditions. Combined with state-of-the-art measurement techniques such as time-resolved PTV, these models allow for precise three-dimensional velocity and wall-shear stress measurements in highly complex patient-specific geometries. Thus, the approach can be utilized to give new insights into disease progression mechanisms, such as flow-induced vascular remodeling or airway collapse.

Acknowledgements The authors gratefully acknowledge the German Research Foundation (Deutsche Forschungsgemeinschaft DFG) for funding this work (project number: 449867589). We also gratefully acknowledge the contribution and support of Trutz Meyer, Nick Capellmann, and the workshop team of the Institute of Aerodynamics during the manufacturing process. The authors are very grateful for the measurement system provided by the Chair and Institute of Aerospace Systems at RWTH Aachen University. The authors are grateful to Dr. František Lízal and his team at Brno University of Technology for providing the three-dimensional digital model geometry of the respiratory tract.

Author contributions B.JM. and M.K. contributed to conceptualization and analysis of results. B.JM. contributed to implementation, experiments, methodology, visualization and writing (original draft and review/editing). M.K. contributed to methodology, supervision, resource and project management and writing (review/editing). All authors read and approved the final version of the manuscript.

Funding Open Access funding enabled and organized by Projekt DEAL. The research was made possible because of the funding from the Deutsche Forschungsgemeinschaft DFG (German Research Foundation) from the project: "Velocity and wall-shear stress measurements of pulsatile flow of blood-analog fluids in elastic vessels", project number: 449867589.

Data availability No datasets were generated or analyzed during the current study.

Code availability Not applicable.

Declarations

Conflict of interest The authors declare no conflict of interest.

Consent to participate Not applicable.

Consent for Publication All authors agreed with the content. The authors and the institute authorities gave explicit consent to submit this article.

Ethical approval Not applicable.

Materials availability Not applicable.

References

Arcaute K, Wicker RB (2008) Patient-specific compliant vessel manufacturing using dip-spin coating of rapid prototyped molds. J Manuf Sci Eng. https://doi.org/10.1115/1.2898839

Biglino G, Verschueren P, Zegels R et al (2013) Rapid prototyping compliant arterial phantoms for in-vitro studies and device testing. J Cardiovasc Magn Reson Off J Soc Cardiovasc Magn Reson 15(1):2. https://doi.org/10.1186/1532-429X-15-2

Bonfanti M, Franzetti G, Homer-Vanniasinkam S (2020) A combined in vivo, in vitro, in silico approach for patient-specific haemodynamic studies of aortic dissection. Ann Biomed Eng 48(12):2950–2964. https://doi.org/10.1007/s10439-020-02603-z

Brindise MC, Rothenberger S, Dickerhoff B et al (2019) Patient-specific cerebral aneurysm hemodynamics: comparison of in vitro volumetric particle velocimetry, computational fluid dynamics (cfd), and in vivo 4d flow mri

Buchmann NA, Atkinson C, Jeremy MC et al (2011) Tomographic particle image velocimetry investigation of the flow in a modeled human carotid artery bifurcation. Exp Fluids 50(4):1131–1151. https://doi.org/10.1007/s00348-011-1042-1

Burgmann S, Große S, Schröder W et al (2009) A refractive index-matched facility for fluid-structure interaction studies of pulsatile and oscillating flow in elastic vessels of adjustable compliance. Exp Fluids. https://doi.org/10.1007/s00348-009-0681-y

Burgmann S, Große S, Schröder W et al (2009) A refractive index-matched facility for fluid-structure interaction studies of pulsatile and oscillating flow in elastic vessels of adjustable compliance. Exp Fluids 47(4):865–881. https://doi.org/10.1007/s00348-009-0681-y

Büsen M, Arenz C, Neidlin M et al (2017) Development of an in vitro piv setup for preliminary investigation of the effects of aortic compliance on flow patterns and hemodynamics. Cardiovasc Eng Technol 8(3):368–377. https://doi.org/10.1007/s13239-017-0309-y

Cherry M, Khatir Z, Khan A et al (2022) The impact of 4d-flow mri spatial resolution on patient-specific cfd simulations of the thoracic aorta. Sci Rep 12(1):15128. https://doi.org/10.1038/s41598-022-19347-6

Cozzi F, Felisati G, Quadrio M (2017) Velocity measurements in nasal cavities by means of stereoscopic piv - preliminary tests. J Phys Conf Ser 882:012010. https://doi.org/10.1088/1742-6596/882/1/012010

Deplano V, Guivier-Curien C, Bertrand E (2016) 3d analysis of vortical structures in an abdominal aortic aneurysm by stereoscopic piv. Exp Fluids. https://doi.org/10.1007/s00348-016-2263-0

Dörner P, Schröder W, Klaas M (2021) Experimental quantification of oscillating flow in finite-length straight elastic vessels for newtonian and non-newtonian fluids. Eur J Mech B Fluids 87:180–195. https://doi.org/10.1016/j.euromechflu.2021.02.001

Fahy P, Delassus P, McCarthy P et al (2014) An in vitro assessment of the cerebral hemodynamics through three patient specific circle of willis geometries. J Biomech Eng 136(1):011007. https://doi.org/10.1115/1.4025778

Farkas Á, Lizal F, Jedelsky J et al (2020) The role of the combined use of experimental and computational methods in revealing the differences between the micron-size particle deposition patterns in healthy and asthmatic subjects. J Aerosol Sci 147:105582. https://doi.org/10.1016/j.jaerosci.2020.105582

Franzetti G, Bonfanti M, Homer-Vanniasinkam S et al (2022) Experimental evaluation of the patient-specific haemodynamics of an aortic dissection model using particle image velocimetry. J Biomech 134:110963. https://doi.org/10.1016/j.jbiomech.2022.110963

Geoghegan PH, Buchmann NA, Spence CJT et al (2012) Fabrication of rigid and flexible refractive-index-matched flow phantoms for flow visualisation and optical flow measurements. Exp Fluids 52(5):1331–1347. https://doi.org/10.1007/s00348-011-1258-0

Ionita CN, Mokin M, Varble N et al (2014) Challenges and limitations of patient-specific vascular phantom fabrication using 3d polyjet printing. Proc SPIE Int Soc Opt Eng 9038:90380M. https://doi.org/10.1117/12.2042266

Janke T, Schwarze R, Bauer K (2017) Measuring three-dimensional flow structures in the conductive airways using 3d-ptv. Exp Fluids. https://doi.org/10.1007/s00348-017-2407-x

Johanning-Meiners BH, Mayolle L, Schröder W et al (2024) Proceedings of the international symposium on the application of laser and imaging techniques to fluid mechanics. In: Proceedings of the international symposium on the application of laser and imaging techniques to fluid mechanics 21:1–13. https://doi.org/10.55037/lxlaser.21st.22

Learoyd BM, Taylor MG (1966) Alterations with age in the viscoelastic properties of human arterial walls. Circ Res 18(3):278–292. https://doi.org/10.1161/01.RES.18.3.278

Lee CS, Tarbell JM (1997) Wall shear rate distribution in an abdominal aortic bifurcation model: effects of vessel compliance and phase angle between pressure and flow waveforms. J Biomech Eng 119(3):333–342. https://doi.org/10.1115/1.2796098

Lee JN, Park C, Whitesides GM (2003) Solvent compatibility of poly(dimethylsiloxane)-based microfluidic devices. Anal Chem 75(23):6544–6554. https://doi.org/10.1021/ac0346712

Li W, Huber GM (2014) Optical characterization of RTV615 silicone rubber compound. J Instrum 9(07):P07012–P07012. https://doi.org/10.1088/1748-0221/9/07/P07012

Lizal F, Elcner J, Jedelsky J et al (2020) The effect of oral and nasal breathing on the deposition of inhaled particles in upper and tracheobronchial airways. J Aerosol Sci 150:105649. https://doi.org/10.1016/j.jaerosci.2020.105649

Mcdougall TJ (1979) On the elimination of refractive-index variations in turbulent density-stratified liquid flows. J Fluid Mech 93(1):83–96. https://doi.org/10.1017/S0022112079001798

Meyer CA, Bertrand E, Boiron O et al (2011) Stereoscopically observed deformations of a compliant abdominal aortic aneurysm model. J Biomech Eng 133(11):111004. https://doi.org/10.1115/1.4005416

Mu LZ, Li XY, Chi QZ et al (2019) Experimental and numerical study of the effect of pulsatile flow on wall displacement oscillation in a flexible lateral aneurysm model. Acta Mech Sin 35(5):1120–1129. https://doi.org/10.1007/s10409-019-00893-8

Nahar K, Gupta N, Gauvin R et al (2013) In vitro, in vivo and ex vivo models for studying particle deposition and drug absorption of inhaled pharmaceuticals. Eur J Pharm Sci Off J Eur Fed Pharm Sci 49(5):805–818. https://doi.org/10.1016/j.ejps.2013.06.004

Najjari MR, Plesniak MW (2018) Secondary flow vortical structures in a 180° elastic curved vessel with torsion under steady and pulsatile inflow conditions. Phys Rev Fluids 3:013101. https://doi.org/10.1103/PhysRevFluids.3.013101

Nof E, Heller-Algazi M, Coletti F et al (2020) Ventilation-induced jet suggests biotrauma in reconstructed airways of the intubated neonate. J R Soc Interface 17(162):20190516. https://doi.org/10.1098/rsif.2019.0516

Olufsen MS, Peskin CS, Kim WY et al (2000) Numerical simulation and experimental validation of blood flow in arteries with structured-tree outflow conditions. Ann Biomed Eng 28(11):1281–1299. https://doi.org/10.1114/1.1326031

Özcan C, Kocatürk Ö, Işlak C et al (2023) Integrated particle image velocimetry and fluid-structure interaction analysis for patient-specific abdominal aortic aneurysm studies. Biomed Eng Online 22(1):113. https://doi.org/10.1186/s12938-023-01179-8

Pielhop K, Schmidt C, Zholtovski S et al (2014) Experimental investigation of the fluid-structure interaction in an elastic 180° curved vessel at laminar oscillating flow. Exp Fluids. https://doi.org/10.1007/s00348-014-1816-3

Pielhop K, Klaas M, Schröder W (2015) Experimental analysis of the fluid-structure interaction in finite-length straight elastic vessels. Eur J Mech B Fluids 50:71–88. https://doi.org/10.1016/j.euromechflu.2014.11.001

Schanz D, Gesemann S, Schröder A (2016) Shake-the-box: Lagrangian particle tracking at high particle image densities. Exp Fluids. https://doi.org/10.1007/s00348-016-2157-1

Schröder A, Willert C, Schanz D et al (2020) The flow around a surface mounted cube: a characterization by time-resolved piv, 3d shake-the-box and lbm simulation. Exp Fluids. https://doi.org/10.1007/s00348-020-03014-5

Soodt T, Pott D, Klaas M et al (2013) Analysis of basic flow regimes in a human airway model by stereo-scanning piv. Exp Fluids. https://doi.org/10.1007/s00348-013-1562-y

Tauwald SM, Erzinger F, Quadrio M et al (2024) Tomo-piv in a patient-specific model of human nasal cavities: a methodological approach. Meas Sci Technol 35(5):055203. https://doi.org/10.1088/1361-6501/ad282c

Weibel ER (1963) Morphometry of the human lung. Springer, Berlin Heidelberg

Wu X, Gürzing S, Schinkel C et al (2022) Hemodynamic study of a patient-specific intracranial aneurysm: comparative assessment of tomographic piv, stereoscopic piv, in vivo mri and computational fluid dynamics. Cardiovasc Eng Technol 13(3):428–442. https://doi.org/10.1007/s13239-021-00583-2

Wu X, Jansen KM, Westenberg JJ et al (2025) Aortic strain, flow pattern and wall shear stress in a patient-specific compliant aorta replica using shake-the-box. Med Eng Phys 135:104263. https://doi.org/10.1016/j.medengphy.2024.104263

Xu X, Wu J, Weng W et al (2020) Investigation of inhalation and exhalation flow pattern in a realistic human upper airway model by piv experiments and cfd simulations. Biomech Model Mechanobiol 19(5):1679–1695. https://doi.org/10.1007/s10237-020-01299-3

Yagi T, Sato A, Shinke M et al (2013) Experimental insights into flow impingement in cerebral aneurysm by stereoscopic particle image velocimetry: transition from a laminar regime. J R Soc Interface 10(82):20121031. https://doi.org/10.1098/rsif.2012.1031

Yazdi SG, Huetter L, Docherty PD et al (2019) A novel fabrication method for compliant silicone phantoms of arterial geometry for use in particle image velocimetry of haemodynamics. Appl Sci 9(18):3811. https://doi.org/10.3390/app9183811

Zhu Z, Ju Y, Zhang C (2020) In-vitro experimental modeling of oscillatory respiratory flow in a ct-scanned osahs tract. Appl Sci 10(22):7979. https://doi.org/10.3390/app10227979

Zimmermann J, Loecher M, Kolawole FO et al (2021) On the impact of vessel wall stiffness on quantitative flow dynamics in a synthetic model of the thoracic aorta. Sci Rep 11(1):6703. https://doi.org/10.1038/s41598-021-86174-6